

See discussions, stats, and author profiles for this publication at: <https://www.researchgate.net/publication/244410154>

# Complex Magnetism and Magnetic Structures of the Metastable $\text{HoMnO}_3$ Perovskite

ARTICLE in INORGANIC CHEMISTRY · FEBRUARY 2001

Impact Factor: 4.76 · DOI: 10.1021/ic0011009

CITATIONS

144

READS

25

6 AUTHORS, INCLUDING:



Angel Muñoz

University Carlos III de Madrid

104 PUBLICATIONS 1,676 CITATIONS

SEE PROFILE



José Antonio Alonso

Spanish National Research Council

484 PUBLICATIONS 7,058 CITATIONS

SEE PROFILE



J. L. Martínez

Spanish National Research Council

195 PUBLICATIONS 2,675 CITATIONS

SEE PROFILE

# Complex Magnetism and Magnetic Structures of the Metastable $\text{HoMnO}_3$ Perovskite

A. Muñoz\*

Departamento de Física, EPS, Universidad Carlos III, Avenida de la Universidad 30, Leganés, E-28911 Madrid, Spain

M. T. Casáis, J. A. Alonso, M. J. Martínez-Lope, and J. L. Martínez

Instituto de Ciencia de Materiales de Madrid, C.S.I.C., Cantoblanco, E-28049 Madrid, Spain

M. T. Fernández-Díaz

Institut Laue-Langevin, BP 156X, 38042 Grenoble Cédex 9, France

Received October 3, 2000

The magnetic properties and the low-temperature magnetic structures of the orthorhombic perovskite  $\text{HoMnO}_3$  (space group  $Pnma$ ) have been studied on polycrystalline samples by magnetization, specific heat, and neutron diffraction measurements. By cooling,  $\text{HoMnO}_3$  exhibits three singularities at  $T_N = 41$  K,  $T \approx 26$  K, and  $T \approx 6.5$  K, suggesting a rich magnetic phase diagram. The neutron diffraction data show that below  $T_N = 41$  K, the  $\text{Mn}^{3+}$  magnetic moments become ordered in an antiferromagnetic arrangement, adopting a modulated sinusoidal magnetic structure characterized by the wave vector  $\mathbf{k} = (k_x, 0, 0)$  ( $k_x = 0.40$  at 41 K) and defined by the magnetic mode  $(C_x, 0, 0)$ . When the temperature is decreased, the propagation vector varies and at  $T \approx 29$  K a transition to a commensurate magnetic structure defined by  $\mathbf{k} = (1/2, 0, 0)$  takes place. Below  $T \approx 22$  K, a small ordered magnetic moment appears on the  $\text{Ho}^{3+}$  cations, strongly increasing below 9 K and reaching  $7.3(1) \mu_B$  at  $T = 1.8$  K. The magnetic structure of the  $\text{Ho}^{3+}$  moments is defined by a  $(A_x, 0, C_z)$  mode. The  $(H, T)$  phase diagram has been mapped out and the different magnetic structures interpreted on the basis of competing superexchange interactions.

## Introduction

The family of perovskite-like oxides  $\text{R}_{1-x}\text{A}_x\text{MnO}_3$  ( $\text{R} = \text{La}$  and first members of the rare earth series;  $\text{A} =$  alkaline earths) has been extensively studied in recent years because these materials show interesting properties such as colossal magnetoresistance or charge-ordering effects.<sup>1–3</sup> As a matter of fact, these perovskites were well-known since 40 years ago; many investigations carried out in the 1950s and 1960s on doped perovskite manganites<sup>4–6</sup> already highlighted the peculiar correlation between magnetism and transport properties. This renewed interest has also spawned numerous studies on the undoped  $\text{RMnO}_3$  perovskites themselves ( $\text{R} = \text{La}$ , rare earths) because they constitute the parent compounds of the above-mentioned hole-doped derivatives. In particular,  $\text{LaMnO}_3$  has been the topic of a number of studies<sup>7–13</sup> addressing the interplay among structure, magnetic, and transport properties. In  $\text{LaMnO}_3$ ,

according to Hund's rules, the electronic configuration of the  $\text{Mn}^{3+}$  ions is  $t_{2g}^3e_g^1$ . The  $e_g$  orbitals are strongly hybridized with the oxygen p orbitals. Besides, a strong distortion of the  $\text{MnO}_6$  octahedra associated with the Jahn–Teller effect<sup>14</sup> is usually present. This distortion<sup>11,15,16</sup> seems to be at the origin of the orbital ordering observed in  $\text{LaMnO}_3$ . In the basal  $ac$  plane, the dominantly populated  $d_{3x^2-r^2}/d_{3z^2-r^2}$  orbitals alternate (space group  $Pnma$ , with  $b$  as the long axis), which gives rise to a ferromagnetic (FM) superexchange interaction between the  $e_g$  orbitals within the plane. As the  $d_{y^2-z^2}$  and  $d_{x^2-y^2}$  orbitals are less populated, the interlayer superexchange interaction is dominated by the interaction through the  $t_{2g}$  orbitals, which is antiferromagnetic (AFM). At low temperatures the breakdown of the 2-fold degeneracy of the  $e_g$  orbitals stabilizes a layered A-type AFM structure (below  $T_N = 130$  K).<sup>4,17</sup>

The behavior of other members of the  $\text{RMnO}_3$  series ( $\text{R} =$  rare earth) has been much less studied. There are only a few reports concerning the crystal and magnetic structures of

\* To whom correspondence should be addressed. E-mail: amunoz@elrond.uc3m.es.

- (1) Kusters, R. M.; Singleton, J.; Keen, D. A.; McGreevy, R.; Hayes, R. *Physica* **1989**, *155B*, 362.
- (2) Van Helmolt, R.; Wecker, J.; Holzapfel, B.; Schultz, L.; Samwer, K. *Phys. Rev. Lett.* **1993**, *71*, 2331.
- (3) Tokura, Y.; Urushibara, A.; Morimoto, Y.; Arima, T.; Asamitsu, A.; Kido, G.; Furukawa, N. *J. Phys. Soc. Jpn.* **1994**, *63*, 3931.
- (4) Wollan, E. O.; Koehler, W. C. *Phys. Rev.* **1955**, *100*, 545.
- (5) Jonker, G. H.; Van Santen, J. H. *Physica* **1950**, *16*, 337.
- (6) Goodenough, J. B. *Phys. Rev.* **1955**, *100*, 564.
- (7) Saitoh, T.; Boucquet, A. E.; Mizokawa, T.; Namatame, H.; Fujimori, A.; Abbate, M.; Takeda, Y.; Takano, M. *Phys. Rev. B* **1995**, *51*, 13942.
- (8) Sarma, D. D.; Shanthi, N.; Barman, S. R.; Hamada, N.; Sawada, H.; Terakura, K. *Phys. Rev. Lett.* **1995**, *75*, 1126.

- (9) Saptathy, S.; Popovic, Z. S.; Vukajlovic, F. R. *Phys. Rev. Lett.* **1996**, *76*, 960.
- (10) Pickett, W. E.; Singh, D. *Phys. Rev. B* **1996**, *53*, 1146.
- (11) Solovyev, I.; Hamada, N.; Terakura, K. *Phys. Rev. Lett.* **1996**, *76*, 4825.
- (12) Hirota, K.; Kaneko, N.; Nishizawa, A.; Endoh, Y. *J. Phys. Soc. Jpn.* **1996**, *65*, 3736.
- (13) Moussa, E.; Hennion, M.; Rodríguez-Carvajal, J.; Moudden, H. *Phys. Rev. B* **1996**, *54*, 15149.
- (14) Kanamori, J. *J. Appl. Phys., Suppl.* **1960**, *31*, 14S.
- (15) Mizokawa, T.; Fujimori, A. *Phys. Rev. B* **1996**, *54*, 5368.
- (16) Ishihara, S.; Inoue, J.; Maekawa, S. *Phys. Rev. B* **1997**, *55*, 8280.
- (17) Koehler, W. C.; Wollan, E. O. *J. Phys. Chem. Solids* **1957**, *2*, 100.

PrMnO<sub>3</sub> and NdMnO<sub>3</sub>.<sup>18</sup> The Pr and Nd terms also exhibit an A-type AFM structure<sup>19</sup> defined by the propagation vector  $\mathbf{k} = 0$ . The Tb analogue, TbMnO<sub>3</sub>, becomes magnetically ordered with a sine-wave incommensurate structure<sup>20</sup> defined by the propagation vector  $\mathbf{k} = (k_x, 0, 0)$ , and YMnO<sub>3</sub> orders according to a helical magnetic arrangement<sup>21</sup> also given by  $\mathbf{k} = (k_x, 0, 0)$ .

It is interesting to point out that for rare earth cations smaller than Tb<sup>3+</sup> the orthorhombic perovskite structure for RMnO<sub>3</sub> is no longer the stable phase under ordinary synthetic conditions<sup>22,23</sup> because a hexagonal nonperovskite phase (space group  $P6_3cm$ )<sup>24</sup> with the same stoichiometry strongly competes in stability from Ho to Lu, Y, and Sc, with a smaller ionic radius. However, hexagonal manganites can be transformed into orthorhombic by annealing under high pressure.<sup>25,26</sup> Also, HoMnO<sub>3</sub> and YMnO<sub>3</sub> can be prepared as metastable phases by working under soft-chemistry conditions.<sup>21,27,28</sup> In the course of our current research on rare earth manganites,<sup>28</sup> we were able to obtain a well-crystallized single-phased HoMnO<sub>3</sub> perovskite, which allowed us to perform a complete study of the magnetic properties of this material, including magnetization, specific heat, and neutron diffraction measurements. In this article we describe the complex low-temperature magnetic behavior of this metastable perovskite and compare the magnetic arrangements with those of other known RMnO<sub>3</sub> perovskites.

## 2. Samples and Experiment

HoMnO<sub>3</sub> was prepared in polycrystalline form from citrate precursors obtained by soft-chemistry procedures. Stoichiometric amounts of analytical grade Ho<sub>2</sub>O<sub>3</sub> and MnCO<sub>3</sub> were dissolved in citric acid by adding several droplets of concentrated HNO<sub>3</sub> to favor the dissolution of the rare earth oxide. An organic resin containing a random distribution of Ho and Mn cations was obtained by slow evaporation of the citrate solution. All the organic materials and nitrates were eliminated in consecutive treatments at 120 °C (6 h), 600 °C (12 h), and 700 °C (12 h) in air. This procedure gave rise to highly reactive precursor materials, amorphous for X-ray diffraction (XRD). A final treatment was designed to prevent or minimize the stabilization of the competitive hexagonal HoMnO<sub>3</sub> phase, thus increasing the yield of the orthorhombic perovskite phase. The amorphous precursor was heated in an O<sub>2</sub> flow from 600 to 900 °C in 12 h and then held at 900 °C for 12 h. This procedure enabled the preparation of a pure HoMnO<sub>3</sub> perovskite. The product was initially characterized by laboratory XRD for phase identification and to assess phase purity. The oxygen content of the sample was determined to be 3.01(1) by thermal analysis under reducing conditions (H<sub>2</sub>/N<sub>2</sub> flow), through total reduction to MnO + Ho<sub>2</sub>O<sub>3</sub>.

Magnetic measurements were performed in a commercial superconducting quantum interference device (SQUID) magnetometer. The dc magnetic susceptibility measurements were done under a magnetic field  $H = 5$  kOe and in the temperature range 2 K <  $T$  < 300 K. The ac susceptibility was measured in an oscillating magnetic field of 997 Hz

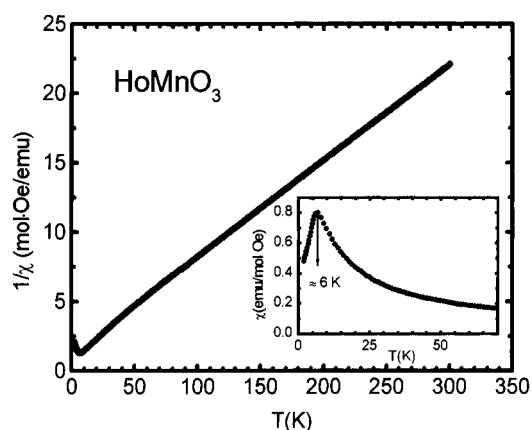


**Figure 1.** Thermal variation of the inverse of the dc susceptibility of HoMnO<sub>3</sub> measured under field-cooling (FC) conditions at  $H = 5$  kOe. Inset: dc susceptibility from 2 to 70 K at  $H = 5$  kOe.

and from  $T = 2$  K to  $T = 70$  K. Isothermal magnetization curves were obtained at different temperatures  $T = 2, 15, 26, 35,$  and  $50$  K and in magnetic fields ranging from  $-50$  to  $50$  kOe.

The specific heat was measured in a semiadiabatic He calorimeter using the heat-pulsed-relaxation method in the temperature interval  $2$  K <  $T$  <  $95$  K and under magnetic fields up to  $90$  kOe.

Neutron powder diffraction (NPD) diagrams were collected at the Institut Laue-Langevin in Grenoble (France). To refine the crystallographic structure, a high-resolution NPD pattern was acquired at room temperature at the D2B high-resolution diffractometer with  $\lambda = 1.594$  Å. A set of NPD patterns were obtained at the D20 high-flux diffractometer in the temperature range from  $1.8$  to  $52$  K, with a  $\lambda = 2.413$  Å wavelength. Data analysis was carried out according to the Rietveld method,<sup>29</sup> and the refinements of both crystal and magnetic structures were performed with the program FULLPROF.<sup>30</sup> In the refinements, the peak shape was simulated by a pseudo-Voigt function and the background was fitted with a 5th-degree polynomial function. The Fermi scattering lengths were  $8.010, -3.730,$  and  $5.803$  fm for Ho, Mn, and O, respectively. The magnetic form factors used were calculated with the coefficients taken from the International Tables.<sup>31</sup> For the Mn<sup>3+</sup> ions the spin-only  $\langle j_0 \rangle$  coefficient was considered; for Ho<sup>3+</sup> the coefficients  $\langle j_0 \rangle$  and  $\langle j_2 \rangle$  were used, corresponding to the dipolar approximation.

## 3. Results from Magnetic and Specific-Heat Measurements

The thermal evolution of the reciprocal dc susceptibility is presented in Figure 1. At temperatures above  $90$  K the susceptibility follows a Curie–Weiss behavior described by an effective paramagnetic moment  $\mu_{\text{eff}} = 10.7(1) \mu_B$  per formula, being the calculated paramagnetic temperature  $\Theta_P$  is  $-17(1)$  K. By considering the theoretical values  $4.9 \mu_B$  for Mn<sup>3+</sup> (spin-only  $S = 2$ ) and  $10.4 \mu_B$  for Ho<sup>3+</sup> and assuming that the total effective moment is given by  $\mu_{\text{total}} = [\mu_{\text{eff}}^2(\text{Mn}) + \mu_{\text{eff}}^2(\text{Ho})]^{1/2}$ , we expect a total magnetic moment of  $\mu_{\text{total}} = 11.50 \mu_B$ . This figure is very close to the experimental value, suggesting that the ground states for both ions are those of the free ion. The negative paramagnetic temperature implies the presence of AFM exchange interactions. The inset of Figure 1 shows the thermal evolution of the dc susceptibility at low temperature. It is characteristic of an AFM behavior with an anomaly at  $T \approx 6$  K. However, in Figure 2, where the imaginary part of the ac susceptibility is reported, an additional anomaly also appears at higher temperatures, around  $40$  K.

- (18) Cherepanov, V. A.; Barkhatova, L. Yu.; Petrov, A. N.; Voronin, V. I. *J. Solid State Chem.* **1995**, *118*, 53.
- (19) Quezel-Ambrunaz, S. *Bull. Soc. Fr. Mineral. Cristallogr.* **1968**, *91*, 339.
- (20) Quezel, S.; Tcheou, F.; Rossat-Mignot, J.; Quezel, G.; Roudaut, E. *Physica* **1977**, *86–88B*, 916.
- (21) Quezel, S.; Rossat-Mignot, J.; Bertaut, E. F. *Solid State Commun.* **1974**, *14*, 941.
- (22) Bertaut, E. F.; Forrat, F. *J. Phys.* **1956**, *17*, 129.
- (23) Gilleo, M. A. *Acta Crystallogr.* **1957**, *10*, 161.
- (24) Yakel, H.; Koehler, W. C.; Bertaut, E. F.; Forrat, F. *Acta Crystallogr.* **1963**, *16*, 957.
- (25) Waintal, A.; Chenavas, J. C. *R. Hebd. Seances Acad. Sci.* **1967**, *264B*, 168; *Mater. Res. Bull.* **1967**, *2*, 819.
- (26) Wood, W. E.; Austin, A. E.; Collins, E. W.; Brog, K. C. *J. Phys. Chem. Solids* **1973**, *34*, 859.
- (27) Brinks, H. W.; Fejllvag, H.; Kjekshus, A. *J. Solid State Chem.* **1997**, *129*, 334.
- (28) Alonso, J. A.; Martínez-Lope, M. J.; Casáis, M. T.; Fernández-Díaz, M. T. *Inorg. Chem.* **2000**, *39*, 917.

(29) Rietveld, H. M. *J. Appl. Crystallogr.* **1969**, *2*, 65.

(30) Rodríguez-Carvajal, J. *Physica* **1993**, *B192*, 55.

(31) *International Tables for Crystallography*; Wilson, A. J. C., Ed.; Kluwer-Academic: London, 1992; Vol. C, p 391.

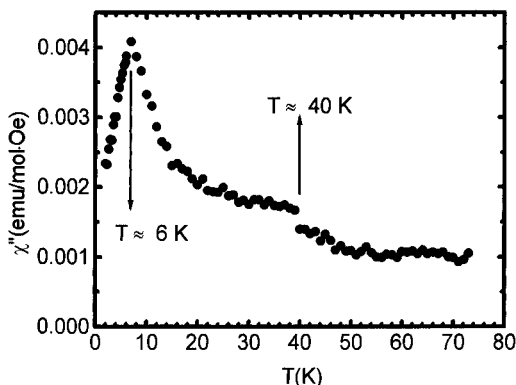


**Figure 2.** Thermal variation of the ac susceptibility for temperatures ranging from 2 to 70 K.

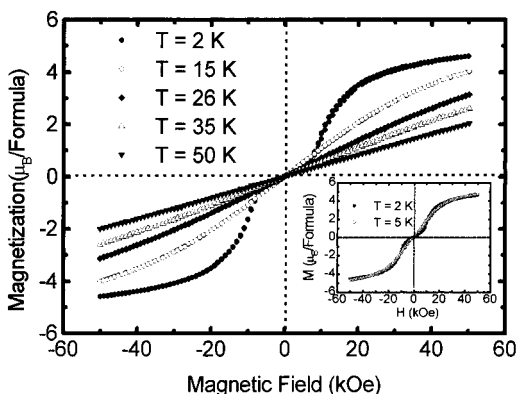


**Figure 3.** Isothermal magnetization curves measured at different temperatures and in fields going from  $-50$  to  $50$  kOe, doing a complete cycle. Inset: isothermal magnetization curves at  $T = 2$  and  $5$  K.

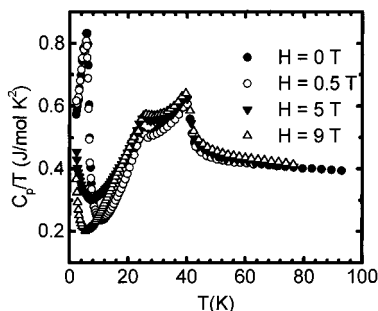


**Figure 4.** Specific-heat measurements for temperatures going from 2 to  $80$  K under several magnetic fields.

Isothermal magnetization curves are presented in Figure 3. After a cycle is completed, no hysteresis phenomena or remnant magnetization were observed. However, a metamagnetic behavior appears at  $T = 2$  K (see inset in Figure 3), which disappears at higher temperatures, at least for fields up to  $50$  kOe. At  $T = 50$  K the magnetization varies linearly with the field, showing a paramagnetic behavior. Finally, no saturation is achieved at  $2$  K for fields up to  $50$  kOe.

The specific-heat data under different magnetic fields are plotted as  $C_p/T$  vs  $T$  in Figure 4. Under zero magnetic field a sharp increase takes place around  $41$  K, indicating the onset of a magnetic order with  $T_N \approx 41$  K, in good agreement with the ac susceptibility. The specific heat exhibits a small shoulder at  $T \approx 26$  K, suggesting the transition to another type of magnetic ordering. As temperature decreases below  $10$  K, the specific-heat curve exhibits a strong peak, showing a maximum at  $T \approx 6.5$  K. This transition coincides with that observed in the susceptibility curve, probably corresponding to the magnetic

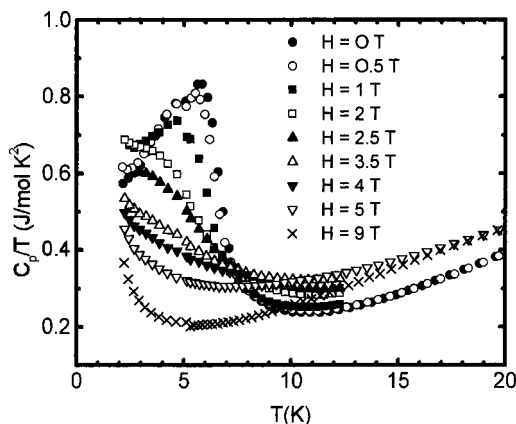


**Figure 5.** Specific-heat data for temperatures going from  $2$  to  $12$  K under several magnetic fields.

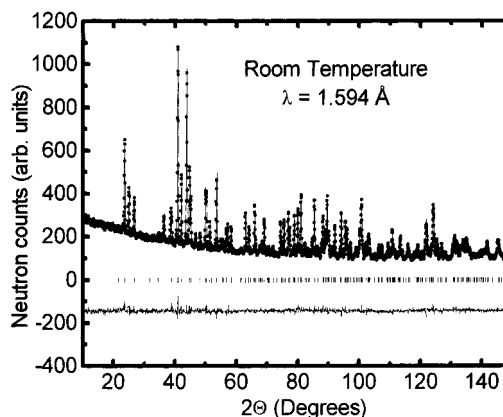


**Figure 6.** Observed (solid circles), calculated (continuous line), and difference (continuous line) NPD patterns of  $\text{HoMnO}_3$ . Bragg reflections are indicated by tic marks.

ordering of the  $\text{Ho}^{3+}$  ions. As is shown in Figures 4 and 5, the effect of an external magnetic field on the three transitions is very different; the transition observed at  $T_N \approx 41$  K is not affected, while the second transition, at  $T \approx 26$  K, is slightly shifted toward higher temperatures, as is expected for an ordered AFM arrangement. In contrast, the transition at  $T \approx 6.5$  K is pushed toward lower temperatures; for fields above  $1$  T this transition is shifted below  $2$  K.

#### 4. Results from Neutron Diffraction Measurements

**4.1. Crystal Structure Refinements.** A high-resolution NPD pattern collected at room temperature with  $\lambda = 1.594$  Å was used to refine the crystallographic structure of  $\text{HoMnO}_3$ . The diagram was indexed in the orthorhombic space group  $Pnma$ , standard setting with the unit-cell parameters  $a = 5.83536(6)$  Å,  $b = 7.36060(8)$  Å, and  $c = 5.25722(5)$  Å. The presence of minor impurity phases was not detected in the diagram. The good agreement between the observed and calculated patterns is presented in Figure 6. The structural parameters and conventional discrepancy factors calculated in the crystallographic analysis are shown in Table 1. The most characteristic geometrical parameters associated with the  $\text{MnO}_6$  octahedra and the  $\text{Ho}-\text{O}$  distances are shown in Table 2. In the  $\text{MnO}_6$  polyhedra the important differences between a long bond distance ( $2.222$  Å) and two short distances ( $1.905$  and  $1.944$  Å) reveal the presence of a strong Jahn–Teller distortion. Besides, the  $\text{Mn}-\text{O}-\text{Mn}$  bonding angles ( $142.47^\circ$  and  $144.08^\circ$ ) very far from  $180^\circ$  imply an important distortion of the perovskite structure through the tilting of the  $\text{MnO}_6$  octahedra.



**Table 1.** Structural Parameters Obtained in the Rietveld Refinement of the NPD Pattern at Room Temperature and with  $\lambda = 1.594$  Å (Space Group *Pnma*)

atom	x	y	z	B (Å <sup>2</sup> )
Ho 4c	0.0839(2)	0.25	0.9825(3)	0.25(3)
Mn 4b	0	0	0.5	0.39(6)
O1 4c	0.4622(4)	0.25	0.1113(4)	0.38(4)
O2 8d	0.3281(3)	0.0534(2)	0.7013(3)	0.45(3)

Unit Cell Dimensions (Å)

 $a = 5.83536(6)$   $b = 7.36060(8)$   $c = 5.25722(5)$   $\text{vol} = 225.807(4)$  Å<sup>3</sup>

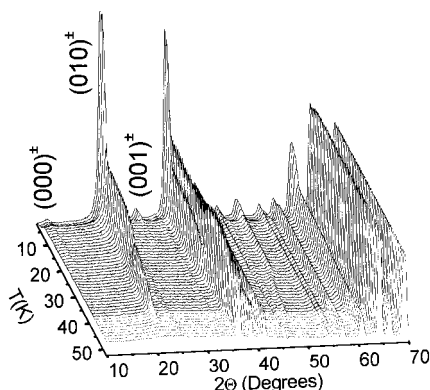
Discrepancy Factors

 $R_p = 3.6\%$   $R_{wp} = 4.5\%$   $R_B = 6.2\%$   $\chi^2 = 1.5$ **Table 2.** Selected Interatomic Distances (Å) and Angles (deg)

Mn distances		Ho distances	
Mn–O1 ( $\times 2$ )	1.9435(10)	Ho–O1	2.2504(28)
Mn–O2 ( $\times 2$ )	1.9046(16)	Ho–O1	2.3090(27)
Mn–O2 ( $\times 2$ )	2.2224(17)	Ho–O2 ( $\times 2$ )	2.2927(20)
$\langle \text{Mn–O} \rangle$	2.0235(6)	Ho–O2 ( $\times 2$ )	2.5118(21)
$\Sigma \text{radii}$	2.016	Ho–O2 ( $\times 2$ )	2.5641(18)
Mn–Mn ( $\times 2$ )	3.6803(1)	$\langle \text{Ho–O} \rangle$	2.4121(8)
Mn–Mn ( $\times 4$ )	3.9271(1)	$\Sigma \text{radii}$	2.386

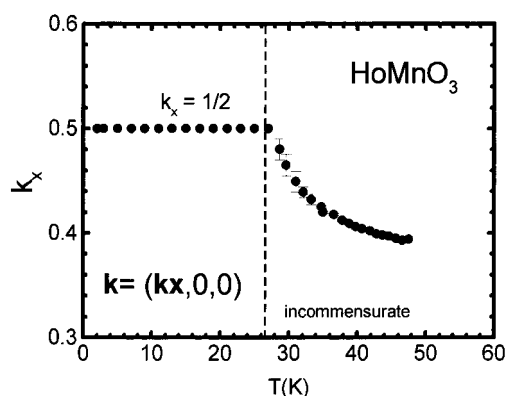
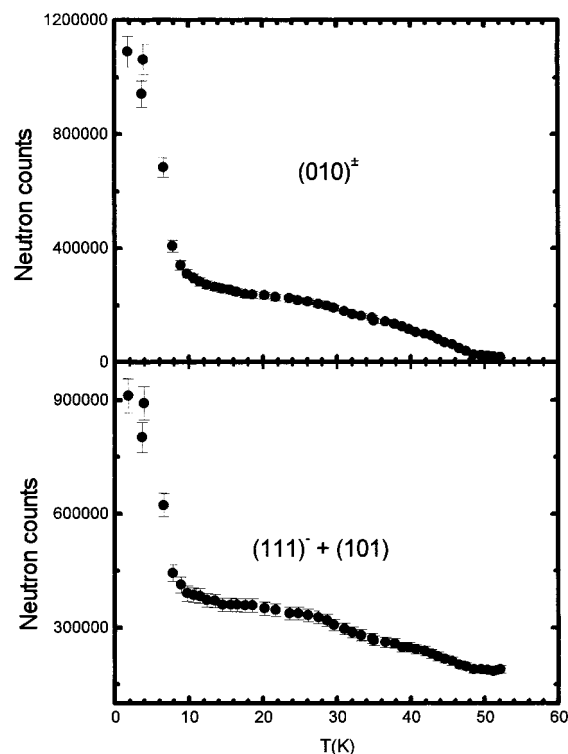
Mn–O–Mn angles

Mn–O1–Mn ( $\times 2$ )	142.47(3)
Mn–O2–Mn ( $\times 4$ )	144.08(6)

**Figure 7.** Thermal evolution of the NPD patterns of HoMnO<sub>3</sub> collected in the D20 high-flux diffractometer with  $\lambda = 2.413$  Å.

The unit-cell lattice parameters verify the relationship  $b/\sqrt{2} \leq c \leq a$ ; as in LaMnO<sub>3</sub>, the strong distortion of the MnO<sub>6</sub> octahedra drives to the so-called O' structure.

**4.2. Magnetic Structure Determination.** To determine the magnetic structure, a set of NPD patterns were acquired from  $T = 1.8$  K to  $T = 52$  K. The evolution of the NPD patterns is shown in Figure 7. When the temperature is decreased below  $T = 47.5$  K, very close to the ordering temperature  $T_N \approx 41$  K, new reflections appear at positions different from those of the Bragg reflections associated with the space group *Pnma*. These new peaks correspond to satellites defined by the propagation vector  $\mathbf{k} = (k_x, 0, 0)$ , which indicates the transition to an incommensurate magnetic structure ( $k_x = 0.40$  at 40 K). Only those  $(h, k, l)^\pm$  satellites with  $k$  odd and  $h + l = 2n$  are observed. As temperature diminishes, the positions of the magnetic peaks vary, implying a change in the  $k_x$  component of the propagation vector. Figure 8 shows the thermal evolution of  $k_x$ . Its value progressively increases and reaches  $k_x = 1/2$  at around  $T \approx 29$  K. This implies the transition to a commensurate magnetic structure defined by  $\mathbf{k} = (1/2, 0, 0)$ . This temperature is concomitant with the anomaly observed in the specific-heat curve at around  $T \approx 26$  K. The new commensurate propagation vector

**Figure 8.** Thermal evolution of the  $k_x$  component of the propagation vector. Below  $T \approx 30$  K,  $\mathbf{k} = (1/2, 0, 0)$ .**Figure 9.** Thermal evolution of the integrated intensities of the magnetic reflections  $(010)^\pm$  and  $(111)^\pm$ .

remains stable down to 1.8 K (Figure 8). In Figure 9, the thermal evolution of the integrated intensities of the satellites  $(010)^\pm$  and  $(111)^\pm$  is plotted. Below  $T = 8.9$  K important changes take place in the NPD pattern: (i) there is a notable increase in the integrated intensities of the magnetic peaks and (ii) the reflection condition  $k$  odd and  $h + l = 2n$  is no longer respected, new satellites appear as  $(000)^\pm$  and  $(001)^\pm$  (see Figures 9 and 10). These changes in the NPD patterns are coincident with the anomaly observed in the specific heat at  $T \approx 6.5$  K.

In the temperature range  $29.6 \text{ K} \leq T \leq 47.5 \text{ K}$ , the refinement of the experimental NPD data is possible if we assume that only the Mn<sup>3+</sup> magnetic moments are ordered. As is indicated in the Appendix, only solutions corresponding to the magnetic mode **C** (the Fourier components verify the relationships  $m_1^k = e^{i\pi k}, m_2^k = -m_3^k = -e^{i\pi k}, m_4^k$ ) are compatible with the extinction rules found in the NPD patterns in this temperature range. After all of the possible solutions are checked, the best agreement with the experimental data is obtained for a modulated sine-wave structure given by the magnetic mode  $(C_x, 0, 0)$ , with the Mn magnetic moments parallel to the  $a$  axis. The Mn<sup>3+</sup>

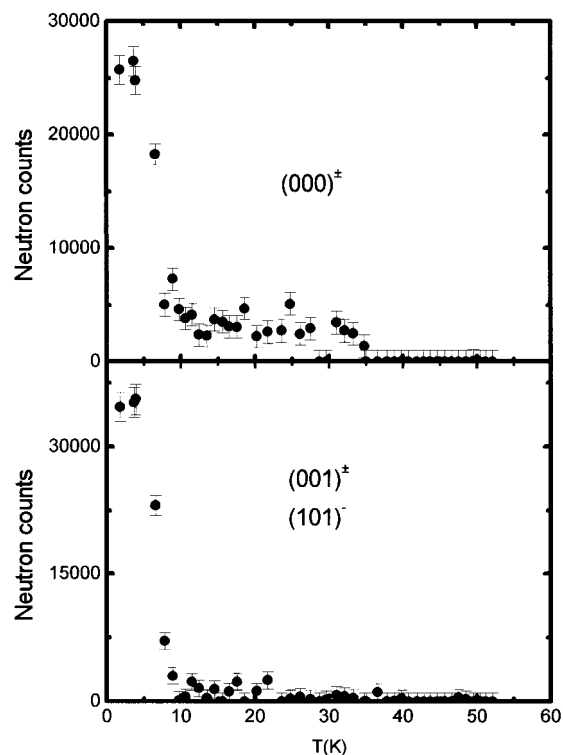


**Figure 10.** Thermal evolution of the integrated intensities of the magnetic reflections  $(000)^\pm$  and  $(001)^\pm$ .

ions, numbered as 1, 2, 3, and 4, are placed respectively at the positions  $(0,0,1/2)$ ,  $(1/2,0,0)$ ,  $(0,1/2,1/2)$ , and  $(1/2,1/2,0)$ . Table 3 presents the magnetic data obtained after the Rietveld refinement was carried out at  $T = 35$  K; the experimental and calculated NPD patterns are compared in Figure 11a.

In the temperature range  $8.9 < T < 29.6$  K, the magnetic structure is commensurate with  $\mathbf{k} = (1/2,0,0)$ . The analysis of the NPD patterns shows that initially only the  $\text{Mn}^{3+}$  ions are ordered with a magnetic structure given by  $(C_x,0,0)$  (the relations between the magnetic moments for  $\mathbf{C}$  are  $\mathbf{m}_1 = \mathbf{m}_2 = -\mathbf{m}_3 = -\mathbf{m}_4$ ). However, below  $T \approx 22$  K, the magnetic moments of Mn atoms reach saturation and it is necessary to consider, additionally, the ordering of the  $\text{Ho}^{3+}$  magnetic moments, which adopt the magnetic structure  $(A_x,0,C_z)$ . At first, the Ho magnetic moments are parallel to the  $x$  direction, and at  $T \approx 13$  K, a component along the  $z$  direction appears. As can be seen in Figure 12, the Ho cations exhibit a small ordered magnetic moment in this region. The  $\mathbf{A}$  magnetic mode implies the relations  $\mathbf{m}_5 = -\mathbf{m}_6 = -\mathbf{m}_7 = \mathbf{m}_8$ , whereby 5, 6, 7, and 8 stand for the Ho atoms located respectively at positions  $(x, 1/4, z)$ ,  $(\bar{x} + 1/2, 3/4, z + 1/2)$ ,  $(\bar{x}, 3/4, \bar{z})$ , and  $(x + 1/2, 1/4, \bar{z} + 1/2)$ . In Table 3 the results from the fitting carried out at  $T = 24.8$  K are presented, and the corresponding experimental and calculated patterns are compared in Figure 11b.

For  $T \leq 8.9$  K, the magnetic structure is similar to that found

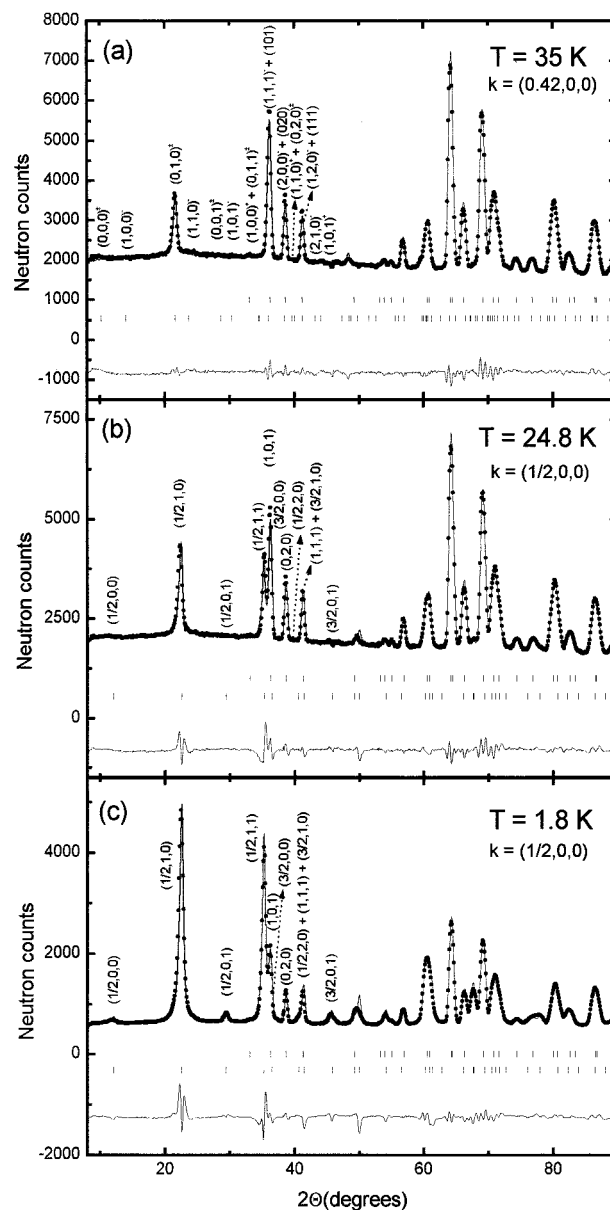


**Figure 11.** Comparison between the observed and calculated NPD patterns by the Rietveld method in the ordered regions: (a)  $T = 35$  K; (b)  $T = 24.8$  K; (c)  $T = 1.8$  K.

for  $8.9 < T < 29.6$  K, with the magnetic arrangement  $(C_x,0,0)$  for Mn and  $(A_x,0,C_z)$  for Ho; below 8.9 K the Ho magnetic moments notably increase, as is shown in Figure 12, reaching the value  $7.27(11) \mu_B$  at  $T = 1.8$  K (see Table 3). In Figure 11c, the experimental and calculated NPD patterns corresponding to  $T = 1.8$  K are plotted. In Figure 13 the different magnetic structures in the distinct ordered regions are represented.

Let us point out that the magnetic structure found for Ho

**Table 3.** Magnetic Data and Discrepancy Factors Corresponding to the Magnetic Structure Refinements Performed at Several Characteristic Temperatures

	$T = 35$ K $\mathbf{k} = (0.420(1),0,0)$		$T = 24.8$ K $\mathbf{k} = (1/2,0,0)$		$T = 1.8$ K $\mathbf{k} = (1/2,0,0)$	
	Mn	Ho	Mn	Ho	Mn	Ho
solution	$(C_x,0,0)$		$(C_x,0,0)$		$(C_x,0,0)$	
moment ( $\mu_B$ )	$(4.00(4),0,0)$		$(3.87(4),0,0)$		$(4.0(2),0,0)$	
$  \vec{m}  $ ( $\mu_B$ )	$A_k/\sqrt{2} = 2.83(2)$		$3.87(4)$		$4.0(2)$	
$R_{\text{Bragg}}$	2.8		3.3		3.3	
$R_{\text{magn}}$	7.5		2.1		6.0	
$\chi^2$	1.2		1.9		2.6	
					$(A_x,0,C_z)$	
					$(6.29(13),0,3.64(10))$	
					$7.27(11)$	

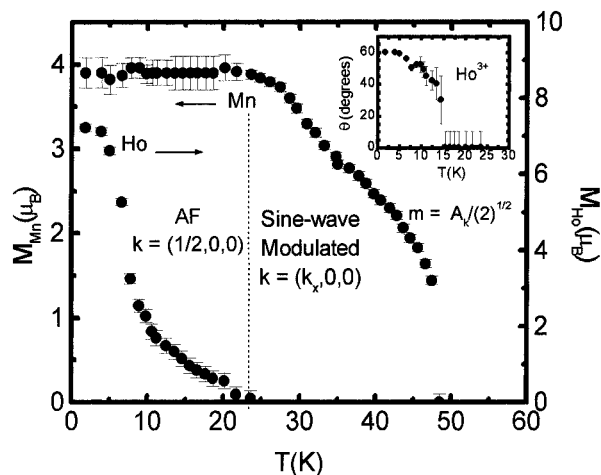


**Figure 12.** Thermal evolution of the magnetic moments for Mn and Ho atoms. For Mn atoms, the average magnetic moment,  $m = A_k/\sqrt{2}$ , is represented in the temperature range  $29.6 \leq T \leq 47.5$  K,  $A_k$  being the sine-wave amplitude. Inset: angle between the Ho magnetic moment and the  $z$  axis.

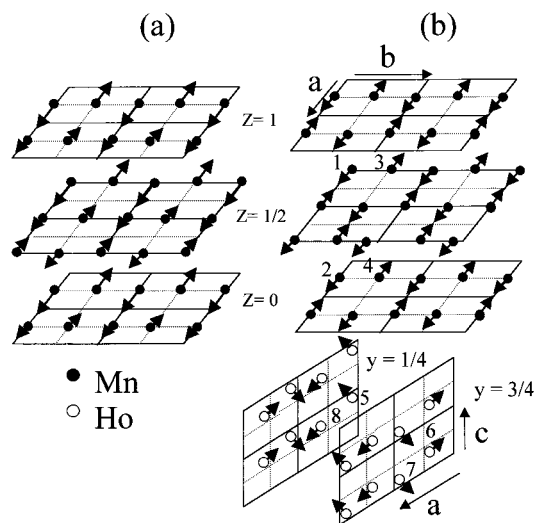


**Figure 13.** Magnetic structure of HoMnO<sub>3</sub>: (a) modulated sine-wave structure for  $29.6 \leq T \leq 47.5$  K; (b) commensurate structure for  $T < 29.6$  K. Ho atoms are only ordered below  $T \approx 20$  K.

atoms,  $(A_x, 0, C_z)$ , cannot be distinguished from the magnetic mode  $(C_x, 0, A_z)$ . It is due to the fact that the magnetic structure factor for Ho,  $\mathbf{F}_{\text{M, Ho}}$ , verifies the relation  $\mathbf{F}_{\text{M, Ho}}(\mathbf{C}) = -\mathbf{F}_{\text{M, Ho}}^*(\mathbf{A})$ . The total magnetic structure factor is  $\mathbf{F}_{\text{M}} = \mathbf{F}_{\text{M, Ho}} + \mathbf{F}_{\text{M, Mn}}$ . Because the new reflections that appear below  $T \leq 8.9$  K do not respect the reflection condition of  $k$  odd and  $h + l = 2n$ , the Mn atoms do not contribute to them, and therefore, for these reflections  $\mathbf{F}_{\text{M}} = \mathbf{F}_{\text{M, Ho}}$ . The magnetic moment for Mn atoms is mainly determined from the new reflections for which it is verified that  $\mathbf{F}_{\text{M}}(\mathbf{C}) \mathbf{F}_{\text{M}}^*(\mathbf{C}) = \mathbf{F}_{\text{M}}(\mathbf{A}) \mathbf{F}_{\text{M}}^*(\mathbf{A})$ .

## 5. Discussion

First, let us discuss the mean features found in the magnetic measurements. In the dc susceptibility curve no changes are observed at the magnetic transitions undergone at 41 K ( $T_N$ ) and at 26 K; this is due to the fact that these transitions only concern Mn<sup>3+</sup> ions, and they are concealed by the larger contribution associated with the paramagnetic behavior of Ho<sup>3+</sup> ions. With respect to the metamagnetic transition observed at  $T = 2$  K, it very possibly involves only Ho<sup>3+</sup> ions. The magnetic ordering of the Mn<sup>3+</sup> ions is uniaxial, parallel to the  $a$  direction,

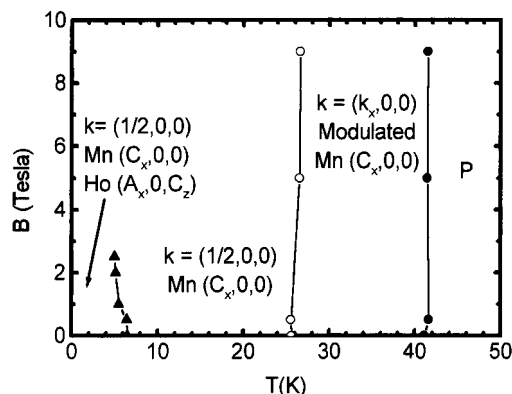


**Figure 14.** Magnetic ( $H, T$ ) phase diagram of HoMnO<sub>3</sub>.

and the moments are not arranged in a layered structure that could lead to field-induced rotations of whole planes. Besides, the metamagnetic transition is observed at low fields, e.g.,  $H \approx 8$  kOe at 2 K, and only at temperatures below 6.5 K. If the Mn atoms were involved, because they are already nearly saturated at 22 K, a metamagnetic transition would be expected to occur at temperatures above 6.5 K, and it would require higher magnetic fields. For Ho<sup>3+</sup> ions the moments lie in the  $(1, 0, 1)$  planes, the spin arrangement being the same for all the planes shifted by an amount  $b$  along the  $b$  direction. Therefore, on applying a magnetic field, the component of the field parallel to the  $(1, 0, 1)$  planes can originate, beyond a critical value, a rotation of the moments toward the field direction, which gives rise to a sudden increase of the magnetization. Neutron diffraction experimental results have emphasized that HoMnO<sub>3</sub> presents a very peculiar evolution of the magnetic structures in comparison with other orthorhombic manganites. Manganese perovskites for the larger rare earth cations, such as LaMnO<sub>3</sub>, PrMnO<sub>3</sub>, and NdMnO<sub>3</sub>, present a commensurate ground-state ordered arrangement, whereas the smaller rare earth perovskites, such as TbMnO<sub>3</sub> and YMnO<sub>3</sub>, seem to order with an incommensurate magnetic structure. We report on the first observation of an incommensurate to commensurate transition for HoMnO<sub>3</sub>.

The main features found in the NPD study, combined with the results of magnetization and specific-heat measurements, are summarized in the phase diagram presented in Figure 14. Four regions can be distinguished. When the paramagnetic state is cooled below  $T \approx 41$  K, formation of a magnetic structure that only involves the Mn<sup>3+</sup> moments is observed; this ordered arrangement is collinear, and the magnitude of the moments is modulated along the  $a$  direction. In HoMnO<sub>3</sub>, below 26 K the  $k_x$  component of the propagation vector adopts a semi-integer commensurate value, which allows us to define a magnetic unit cell by doubling the chemical one along the  $a$  direction. In fact, the high-temperature magnetic structure can be interpreted as a modulation of the commensurate magnetic structure found below 26 K. Finally, below  $T = 6.5$  K the Ho<sup>3+</sup> magnetic moments also become ordered with the same propagation vector but a different, noncollinear arrangement  $(A_x, 0, C_x)$ . The boundary of this low-temperature region is significantly field-dependent because of the sensitivity of the Ho<sup>3+</sup> noncollinear structure to the external magnetic field.

It is worth discussing in more detail two features of this magnetic phase diagram: (i) the microscopic origin of the AF arrangement in the  $ac$  plane and (ii) the origin of the incommensurability found immediately below the Néel temperature. With respect to the first issue, it is noteworthy that the same kind of magnetic structure has been observed for TbMnO<sub>3</sub> in all of the temperature ranges down to 1.8 K, exhibiting the same

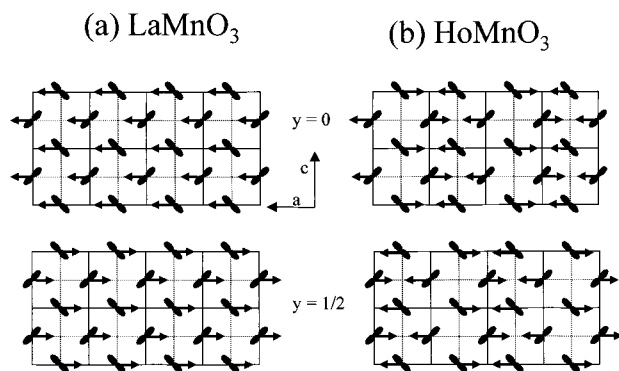


**Figure 15.** Magnetic ordering of the Mn sublattices of  $\text{RMnO}_3$  typified for  $\text{R} = \text{La}$  and  $\text{R} = \text{Ho}$  (in the commensurate region).

orientation along the  $a$  axis of the Mn magnetic moments. For  $\text{YMnO}_3$  a helical magnetic structure<sup>21</sup> had been described, but a careful examination of good-quality NPD data clearly shows, again, the stabilization of a  $(C_x, 0, 0)$  magnetic structure characterized by a propagation vector  $(0.44(1), 0, 0)$ .<sup>32</sup> Thus, this AF arrangement seems to be the stable ground state for small-sized rare earth manganese perovskites. Along the series of  $\text{RMnO}_3$  perovskites and regarding the spin arrangement in the  $ac$  plane, two significantly different magnetic structures have been reported: the intralayer FM coupling for  $\text{R} = \text{La}$ ,  $\text{Pr}$ , and  $\text{Nd}$ ; and the AFM arrangement for  $\text{R} = \text{Tb}$ ,  $\text{Y}$ , and  $\text{Ho}$ . There is a lack of information about the magnetic structures of the intermediate terms for  $\text{R} = \text{Sm}$ ,  $\text{Eu}$ , and  $\text{Gd}$ , given the large neutron absorption cross sections of these rare earths, and this has so far prevented the corresponding NPD study. Both kinds of magnetic arrangements are schematically represented in Figure 15, illustrated for  $\text{R} = \text{La}$  and  $\text{R} = \text{Ho}$ . Let us point out that in all the series the magnetic anisotropy aligns the Mn magnetic moments along the  $a$  direction. In the first case (large R cations; e.g.,  $\text{R} = \text{La}$ ), the magnetic coupling between neighboring Mn moments within Mn–O layers perpendicular to the  $b$  axis ( $Pnma$  setting) is FM, being that the adjacent layers are coupled antiferromagnetically; that means four FM and two AFM magnetic couplings for each Mn moment. In the second case (small R cations; e.g.,  $\text{R} = \text{Ho}$ ), the magnetic coupling within each layer can be described as AFM with two neighboring Mn cations and as FM with the other two. Adjacent layers are also antiferromagnetically coupled; that means two FM and four AFM magnetic couplings for each Mn moment. The magnetic structure typified by  $\text{LaMnO}_3$  has been interpreted as a result of the orbital ordering of  $e_g$  orbitals within each layer, giving rise to four FM interactions, according to the Goodenough–Kanamori<sup>6</sup> rules. This orbital ordering is also represented in Figure 15, where only the  $d_{3z^2-r^2}$  orbitals are depicted for the sake of simplicity. The same kind of orbital ordering is presumably present in  $\text{HoMnO}_3$  because the structural data (defined in the same space group) indicate a strong deformation of the  $\text{MnO}_6$  octahedra, symptomatic of a cooperative Jahn–Teller distortion. The distortion of the octahedra has been quantified to be approximately the same as that found in  $\text{Pr}$  and  $\text{Nd}$  perovskites and slightly higher than that present in  $\text{LaMnO}_3$ .<sup>28</sup> Detailed structural studies show that the degree of orbital ordering remains almost unchanged for the last terms of the series ( $\text{R} = \text{Tb}$ ,  $\text{Ho}$ ,  $\text{Er}$ ,  $\text{Y}$ ).<sup>28</sup> However, there is a factor that regularly increases along the series and is probably the cause of the differences found in the magnetic structures; the tilting of the  $\text{MnO}_6$  octahedra,  $\omega$ , defined as  $\omega = (180 - \langle \text{Mn–O–Mn} \rangle)/2$ , increases from  $24.8^\circ$  for  $\text{R} = \text{La}$  to  $34.7^\circ$  for  $\text{R} = \text{Tb}$  and finally to  $36.5^\circ$  for  $\text{R} = \text{Ho}$ . The validity of the Goodenough rules,<sup>6</sup> dictating an FM interaction between occupied  $d_{3z^2-r^2}$  orbitals rotated by  $90^\circ$ , requires a superexchange Mn–O–Mn angle close to  $180^\circ$ . For  $\text{HoMnO}_3$ , the  $\langle \text{Mn–O–Mn} \rangle$  angle within the  $ac$  layers is  $144.1^\circ$ , which probably spoils the overlapping between Mn and O orbitals required to ensure the FM interaction with all four neighboring Mn atoms. The weakening of the interactions to the nearest neighbors probably makes it possible that next-nearest neighbor interactions become important in the Hamiltonian determining the stable ground state, as will be discussed in the Appendix. The second issue, related to the origin of the incommensurate ordering at  $T_N = 41$  K, is also probably in connection with the weakening of the direct superexchange interactions due to the steric distortion of the perovskite structure. As a rule, a modulation of a magnetic structure in insulator materials is caused by exchange interactions with different signs between the nearest neighbors and next-nearest neighbors, as discussed in the Appendix. Also, it seems that there are other mechanisms that can cause an incommensurate magnetic structure. Recently, a Dzyaloshinskii–Moriya<sup>33,34</sup> (DM) term has been invoked to explain the incommensurate magnetic spiral structure in  $\text{Ba}_2\text{CuGe}_2\text{O}_7$ .<sup>35,36</sup> However, in this compound the deviation from the commensurate structure is very small, whereas in  $\text{HoMnO}_3$  the deviation is bigger (for instance,  $k = (0.40, 0, 0)$  at  $T = 40$  K). Let us point out that although  $\text{HoMnO}_3$  is centrosymmetric, the DM terms are nonzero for next-neighbors Mn atoms.<sup>11</sup>

With respect to the ordering of the  $\text{Ho}^{3+}$  moment ions, a small ordered magnetic moment appears below 22 K that notably increases below 9 K. The ordering of  $\text{Ho}^{3+}$  moments could either be caused, in principle, by polarization from the exchange field of Mn moments or be driven by direct superexchange Ho–O–Ho interactions. Let us analyze both possibilities. The Ho atoms are placed between two planes of Mn octahedra, each Ho being surrounded by eight nearest Mn atoms. The magnetic structure of the Mn atoms,  $(C_x, 0, 0)$ , is invariant under the symmetry element  $\bar{2}_y(0, 1/2, 0)$ , which is placed at the positions of the Ho atoms; therefore, the eight nearest Mn atoms are divided into four groups of two equivalent Mn atoms with opposite magnetic moments. According to the mean-field approximation, this environment would give rise to a zero polarization at the Ho site. Thus, the ordering of the  $\text{Ho}^{3+}$  moments should mainly be due to the direct Ho–O–Ho interactions. These interactions are, presumably, rather strong given the large magnetic moment of  $\text{Ho}^{3+}$  cations. This situation is different from that observed in other rare earth perovskites in which the polarization of the rare earth cation by the exchange field of the transition-metal sublattice is the key factor in understanding the ordering of the rare earth moments. An example is the behavior of  $\text{NdNiO}_3$ <sup>37</sup> in which the Nd ordering is caused by the Nd–Ni exchange interaction, implying that only a half of the Nd atoms are ordered, the other half exhibiting a paramagnetic ground state.

## 6. Conclusion

The combination of NPD, magnetization, and specific-heat techniques has allowed us to establish the magnetic phase

(33) Dzyaloshinskii, I. E. *JETP* **1964**, *46*, 1420.

(34) Moriya, T. *Phys. Rev.* **1960**, *120*, 91.

(35) Zheludev, A.; Shirane, G.; Sasago, Y.; Koide, N.; Uchinokura, K. *Phys. Rev. B* **1996**, *54*, 15163.

(36) Zheludev, A.; Maslov, S.; Shirane, G.; Sasago, Y.; Koide, N.; Uchinokura, K. *Phys. Rev. Lett.* **1997**, *78*, 4857.

(37) García-Muñoz, J. L.; Rodríguez-Carvajal, J.; Lacorre, P. *Phys. Rev. B* **1994**, *50*, 978.

(32) Muñoz, A.; Alonso, J.A. Unpublished results.



diagram of HoMnO<sub>3</sub> perovskite, which shows four distinct regions. Below the paramagnetic state, at  $T_N = 41$  K an incommensurate AFM ordering crystallizes, consisting of a sinusoidal modulated magnetic structure concerning only the Mn<sup>3+</sup> magnetic moments; it is characterized by the wave vector  $\mathbf{k} = (k_x, 0, 0)$  ( $k_x = 0.4$  at 41 K) and defined by the magnetic mode ( $C_x, 0, 0$ ), with the Mn magnetic moments parallel to the  $x$  direction. This structure is stable down to  $T \approx 26$  K, although the propagation vector continuously evolves in this region, finally adopting the commensurate value  $\mathbf{k} = (1/2, 0, 0)$  at 26 K. The commensurate magnetic structure, also defined by the magnetic mode ( $C_x, 0, 0$ ), is stable down to 1.5 K. Besides, below  $T \approx 22$  K, Ho<sup>3+</sup> magnetic moments also become ordered, adopting an arrangement ( $A_x, 0, C_z$ ) superimposed onto the ordered Mn sublattice. The magnetic ordering in Ho<sup>3+</sup> ions is associated with Ho–O–Ho superexchange interactions. The analysis of the structural data reveals a strong orbital ordering effect driven by a cooperative Jahn–Teller distortion. Despite this, the observed magnetic ordering of the Mn sublattice is in contrast with that found for the former members of the RMnO<sub>3</sub> series (R = La, Pr, Nd), AFM of A-type, considered to be a consequence of the orbital ordering. The stabilization of the ( $C_x, 0, 0$ ) mode, also observed in the Tb and Y members, is probably related to the strong steric distortion of the structure given by the small size of the R cation. The significant bending of the Mn–O–Mn angles prevents or reduces the strength of the expected FM couplings between nearest neighbors, enabling the interactions from next-nearest neighbors to play a nonnegligible role in the stabilization of the final magnetic structure.

## Appendix

**Magnetic Structures and Classical Isotropic Exchange Energy.** In this appendix we will discuss the possible magnetic structures compatible with the crystal symmetry, obtained through the group theory analysis following the method described by Bertaut.<sup>38</sup> We will also examine, within the classical framework of the Heisenberg Hamiltonian, under what conditions the existence of an incommensurate magnetic structure is possible in HoMnO<sub>3</sub>.

Experimental results have shown that below  $T_N$  only Mn magnetic moments become ordered; therefore, only the magnetic modes associated with the Mn atoms will be necessary to discuss the stability conditions at the ordering temperature. The magnetic modes are given by the basis vectors of the irreducible representations of the little group  $G_k$ , which is formed by those elements of the space group  $Pnma$  that leave  $\mathbf{k}$  invariant. For  $\mathbf{k} = (k_x, 0, 0)$ ,  $G_k$  is formed by the elements  $h_1/(0, 0, 0)$ ,  $h_2/(1/2, 1/2, 1/2)$ ,  $h_{27}/(0, 1/2, 0)$ , and  $h_{28}/(1/2, 0, 1/2)$ , in Kovalev's notation.<sup>39</sup> By considering the irreducible representations of the group  $G_k$  given by Kovalev<sup>39</sup> and after by use of the projection method, the different basis vectors were determined (see Table 4). The extinction rules derived for the basis vectors are also reported in Table 4.

The classical isotropic exchange energy in the ordered state is given by

**Table 4.** Basis Vectors Corresponding to Mn Atoms for  $\mathbf{k} = (k_x, 0, 0)$  ( $a = e^{-izk_x}$ )

	Mn(1) (0, 0, 1/2)	Mn(2) (1/2, 0, 0)	Mn(3) (0, 1/2, 1/2)	Mn(4) (1/2, 1/2, 0)
$\Gamma_1$	(111)	$a^*(\bar{1}, \bar{1}, 1)$	$(\bar{1}, 1, \bar{1})$	$a^*(1, \bar{1}, \bar{1})$
$\Gamma_2$	(111)	$a^*(1, 1, \bar{1})$	$(1, \bar{1}, 1)$	$a^*(\bar{1}, 1, 1)$
$\Gamma_3$	(111)	$a^*(1, 1, 1)$	$(1, 1, 1)$	$a^*(\bar{1}, 1, 1)$
$\Gamma_4$	(111)	$a^*(\bar{1}, 1, 1)$	$(1, \bar{1}, 1)$	$a^*(1, 1, 1)$
basis vectors		permitted reflections		
$\mathbf{C} = \mathbf{m}_1^k + a^*\mathbf{m}_2^k - \mathbf{m}_3^k - a^*\mathbf{m}_4^k$		$k = 2n + 1$	$h + l = 2n$	
$\mathbf{A} = \mathbf{m}_1^k - a^*\mathbf{m}_2^k - \mathbf{m}_3^k + a^*\mathbf{m}_4^k$		$k = 2n + 1$	$h + l = 2n + 1$	
$\mathbf{F} = \mathbf{m}_1^k + a^*\mathbf{m}_2^k + \mathbf{m}_3^k + a^*\mathbf{m}_4^k$		$k = 2n$	$h + l = 2n$	
$\mathbf{G} = \mathbf{m}_1^k - a^*\mathbf{m}_2^k + \mathbf{m}_3^k - a^*\mathbf{m}_4^k$		$k = 2n$	$h + l = 2n + 1$	

$$\frac{E(\mathbf{k})}{N} = - \sum_{ij} J_{ij}(\mathbf{k}) \mathbf{m}_i^k \cdot \mathbf{m}_j^{-k} \quad (1)$$

where  $J_{ij}(\mathbf{k})$  are the elements of the matrix  $\mathbf{J}(\mathbf{k})$  and represent the Fourier transform of the exchange integrals,

$$J_{ij}(\mathbf{k}) = \sum_{R_n - R_m} J_{ij} e^{-i2\pi\mathbf{k} \cdot (\mathbf{R}_n - \mathbf{R}_m)} \quad (2)$$

$R_n$  and  $R_m$  are lattice translations, and  $i$  and  $j$  refer to the individual spin in the unit cell. The minimum of eq 1 that gives the structure at  $T_N$  defined by the propagation vector  $\mathbf{k} = (k_x, 0, 0)$  is obtained from the following matrix equation:

$$[\mathbf{J}(\mathbf{k}) - \lambda(\mathbf{k})]\mathbf{m}^k = 0 \quad (3)$$

The minimum of the energy is given for the largest eigenvalue of  $\mathbf{J}(\mathbf{k})$ ,  $\lambda(\mathbf{k}_0)$  as

$$\frac{E(\mathbf{k}_0)}{N} - \lambda(\mathbf{k}_0)S^2 \quad (4)$$

For the basis vector  $\mathbf{C}$ , the corresponding eigenvalue is

$$\lambda(\mathbf{k}_0) = 2J_{11} + 2J'_{11} \cos(2\pi k_x) - 2J_{13} + 4J_{12} \cos(\pi k_x) - 8J_{14} \cos(\pi k_x) \quad (5)$$

where the exchange parameters are defined taking as reference the Mn(1) atom, as is reported in Table 5. The eigenvalue given by eq 5 is the largest one if  $J_{13} < 0$  and  $2J_{14} - J_{12} < 0$ . The maximum of  $\lambda(k_x)$  is obtained in a straightforward way ( $d\lambda(k_x)/dk_x = 0$  and  $d^2\lambda(k_x)/dk_x^2 < 0$ ).  $k_x = 0$  and  $\cos(\pi k_x) = (2J_{14} - J_{12})/(2J'_{11})$  are the  $k_x$  values for which  $\lambda(\mathbf{C})$  is a maximum. However, if  $J'_{11} < 0$  and  $2J_{14} - J_{12} < 2J'_{11}$ ,  $\cos(\pi k_x) = (2J_{14} - J_{12})/(2J'_{11})$  gives the maximum value of  $\lambda(\mathbf{C})$ . When  $2J_{14} = J_{12}$ , the propagation vector reaches the value  $\mathbf{k} = (1/2, 0, 0)$ . The energies for the different propagation vectors are

$$\frac{E(\mathbf{k}=0)}{NS^2} = -2J_{11} - 2J'_{11} + 2J_{13} + 4(2J_{14} - J_{12}) \quad (6a)$$

$$\frac{E(\mathbf{k}=(k_x, 0, 0))}{NS^2} = -2J_{11} + 2J'_{11} + 2J_{13} + \frac{(2J_{14} - J_{12})^2}{J'_{11}} \quad (6b)$$

$$\frac{E(\mathbf{k}=(1/2, 0, 0))}{NS^2} = -2J_{11} + 2J'_{11} + 2J_{13} \quad (6c)$$

In LaMnO<sub>3</sub>, the spin wave dispersion measurements<sup>12,13</sup> have shown that the next-nearest-neighbors parameters are negligible

(38) Bertaut, E. F. *Magnetism*; Rado, G. T., Shul, H., Eds.; Academic: New York, 1963; Vol. III, Chapter 4, p 149.

(39) Kovalev, O. V. *Representations of the crystallographic space groups*; Stokes, H. T., Hatch, D. M., Eds.; Gordon and Breach: London, 1993.

**Table 5.** Exchange Parameters and Exchange Paths for Mn Atoms<sup>a</sup>

exchange param	distance	exchange path
$J_{13}$	3.6803(1)	Mn—O1—Mn
$J_{12}$	3.9271(1)	Mn—O2—Mn
$J_{11}$	5.25722(5)	Mn—O2—O2—Mn
$J_{14}$	5.38210(10)	Mn—O1—O1—Mn
$J'_{11}$	5.83536(6)	Mn—O2—O2—Mn

<sup>a</sup> Mn(1) atom has been taken as reference.

in comparison with the nearest-neighbors parameters  $J_{13}$  and  $J_{12}$ . In this case, the eigenvalue for the basis vector **C** is

$$\lambda(\mathbf{k}_0) = -2J_{13} + 4J_{12} \cos(\pi k_x) \quad (7)$$

The maximum of  $\lambda$  takes place for  $k_x = 0$  and for  $J_{13} < 0$  and  $J_{12} > 0$ , which explains the magnetic structure found in LaMnO<sub>3</sub>. In HoMnO<sub>3</sub>, according to eq 5, an incommensurate

magnetic structure defined by  $(k_x, 0, 0)$  would not be possible if only the exchange parameters  $J_{13}$  and  $J_{12}$  are taken into consideration. At least, the next-nearest-neighbors parameters  $J'_{11}$  and  $J_{14}$  should also be considered. For LaMnO<sub>3</sub>, according to Rodríguez-Carvajal et al.,<sup>40</sup> the bonding distances (1.9680, 1.907, 2.178 Å) and the bonding angles (155.48° for Mn—O1—Mn and 155.11° for Mn—O2—Mn) are in contrast with the much bent angles determined for HoMnO<sub>3</sub> (see Table 2). The exchange parameters  $J_{13}$  and  $J_{12}$  in HoMnO<sub>3</sub> are much weaker than those found in LaMnO<sub>3</sub> (as suggested by the much lower Néel temperature of the former compound), and as a consequence,  $J'_{11}$  and  $J_{14}$  become important, explaining the incommensurability of the structure.

IC0011009

(40) Rodríguez-Carvajal, J.; Hennion, M.; Moussa, F.; Moudden, A. H.; Pinsard, L.; Revcolevschi, A. *Phys. Rev. B* **1998**, *57*, R3189.